RAP CONFERENCE PROCEEDINGS, VOL. 10, PP. 21–27, 2025
ISSN 2737-9973 (ONLINE) | DOI: 10.37392/RAPPROC.2025.05
RAP-PROCEEDINGS.ORG

EXAMINING LESION VISIBILITY OF THICK COMPRESSED BREASTS UNDER DIFFERENT IONIZING RADIATION EXPOSURE CONDITIONS BY USING A MAMMOGRAPHIC MATHEMATICAL PHANTOM

Spyridoula Katsanevaki, Nektarios Kalyvas*, Christos Michail, Ioannis Valais, George Fountos, Ioannis Kandarakis

Radiation Physics, Materials Technology and Biomedical Imaging Laboratory,
Department of Biomedical Engineering, University of West Attica, Egaleo, Athens, Greece

Abstract. *Mammography is an X-ray imaging application used for breast diagnosis. Its high importance is denoted by the routinely mammographic examinations suggested for women above a certain age. In the era of digital mammography, various dedicated detector designs have been considered for possible use in a mammographic system. Despite, the detector characteristics the image of thick or dense breasts is a challenge since the amount of radiation transmitted through the breast and incident at the detector surface is a function of the ionizing radiation energy and exposure. In addition, possible breast lesions may be visible or not depending upon their size and composition. In general, a large size and high atomic number lesion has higher visibility than a small size and low atomic number one. A simple mathematical breast phantom was designed which was comprised from breast tissue as a background material and areas corresponding to a) blood for low atomic number material and b) Ca for a high atomic number material like microcalcifications. The phantom dimensions were 1000×1000 pixels, while the lesions were constructed as squares ranging from 2x2 pixels up to 50×50 pixels and lines. The breast thicknesses considered were 5.2 cm and 6 cm for the phantom. For the Ca the thicknesses ranged from 0.0008 cm up to 0.01 cm and for the blood lesions from 0.08 cm up to 0.5 cm. Simulations of the irradiated with 22 keV and 28 keV X-ray photons for different photon fluences, which after transmission from the phantom they have been assumed to impinge a Dexela mammographic detector, have been performed. It was found that at 22 keV and 6 cm breast thickness the 0.003 cm, 10×10 Ca lesion could be observed as well as the 20×20 blood lesion of 0.2 cm thickness. The increase of photon fluence improved the derived image due to the decrease of the image noise levels. The 5.2 cm thickness irradiation conditions produced less noisy images due to the higher number of photons impinging on the detector surface.*

Keywords: *mathematical phantom, image quality, point spread function*

1. INTRODUCTION

X-ray mammography is widely used as the basic mean for detecting breast cancer. All women are instructed to have a mammographic examination when reaching a certain age, usually above 40 years old [1]. The produced mammographic image should pertain enough clarity so as the breast anatomy as well as suspected lesions like microcalcifications to be visible. Towards this aim, specialized detectors have been developed for breast imaging. In addition, the X-ray energy used has been optimized for breast anatomy and thickness. The maximum available X-ray tube voltage of a mammographic machine does not exceed 40 kVp. A prerequisite for high-quality mammographic images is the use of detectors with high resolution and signal-to-noise ratio (SNR) properties [2].

A difficult situation in mammography is imaging of thick breasts. In these cases, the SNR of the detector and the lesion visibility is reduced, since the largest portion of X-rays is absorbed within the breast, without contributing to the final image. A way to overcome this is to use the higher scales of the available kVp of the mammographic machine.

The efficiency of the clinically available detectors in producing images with diagnostic quality is tested with physical phantoms, where the produced images can be used for quantifying the detector performance. However, in cases of experimental detectors, or small size novel detector configurations, software phantoms may be a solution for the theoretical examination of the detector performance. In current literature the development of Monte Carlo based theoretical phantoms have been reported as well as, simple mathematical phantoms have been reported to theoretically test the performance of a novel small pixel detector [3], [4].

In this work the simple theoretical method previously reported has been implemented to examine the image derived by a state-of-the art mammographic detector [5], under exposure conditions corresponding to a thick compressed breast.

2. MATERIALS AND METHODS

2.1. Phantom design

A simple mathematical array of 1000×1000 pixels corresponding to a compressed breast phantom geometry was designed in Matlab software [6]. The phantom consisted of breast tissue, as a background material. In the phantom, squares and lines with

* nkalyvas@uniwa.gr

reducing dimensions were considered. More specifically, the squares were 50×50, 40×40, 30×30, 20×20, 10×10, 4×4 and 2×2 pixels. The corresponding lines widths range from 10 pixels for the large square to 1 pixel for the low dimension squares. The squares and the lines were regarded as blood and Ca, to simulate microcalcifications. A pre-irradiation image of the phantom is shown in Figure 1.

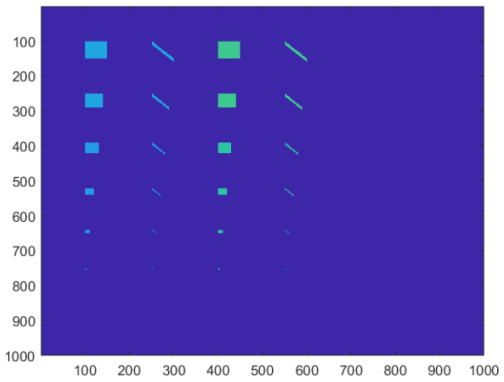

Figure 1. The simulated mathematical phantom. The first two columns are corresponding to the blood lesions and the third and fourth to the Ca lesions.

The thicknesses of the lesions in the dimension of X-ray propagation varied from 0.01 cm to 0.0008 cm for the microcalcifications and from 0.5 cm to 0.008 cm for blood. The phantom thicknesses considered were 5.2 cm and 6 cm, to simulate a thick compressed breast.

2.2. Irradiation conditions

The phantom was mathematically irradiated with monoenergetic X-rays of energies 22 keV and 28 keV. The X-ray fluence values considered were 4.5×10^6 photons/mm², 6.0×10^6 photons/mm² and 9.0×10^6 photons/mm². For each energy E, and X-ray fluence Φ, the exposure, X in mR, incident on the simulated mathematical phantom was calculated as [4]:

$$X = 1.83\times10^{-6}\Phi\times E\times\left(\frac{\mu}{\rho}\right)_{en,air} \qquad (1)$$

Where $(\mu/\rho)_{en,air}$ is the mass energy absorption coefficient of air for energy E. If T is the breast thickness, then the radiation exposure incident on the detector, after the breast has been calculated by multiplying equation 1 with $e^{-\mu_1\times T}$ [2] where μ_1 is the linear attenuation coefficient of the breast tissue. If the X-ray was incident on a pixel, with lesion thickness t and attenuation coefficient μ_2, then Equation 1 was multiplied by $e^{-\mu_1\times(T-t)}e^{-\mu_2\times t}$. The corresponding calculated exposure was multiplied by 8.7 to convert mR in air KERMA, K, with units of μGy. The attenuation coefficients used for the final calculation of K were obtained from XmuDat software [7].

2.3. Image simulation procedure

If the air KERMA, K, to mean pixel value (MPV) conversion function MPV(K) is known, then the calculated K values can be converted into MPV values. The image generation procedure in a detector creates noise in the final image. This noise is studied via the Normalized Noise Power Spectrum (NNPS), which is calculated in spatial frequency domain. Assuming normal statistics the Coefficient of Variation (CV) of the signal can be calculated as [4]:

$$CV = \sqrt{\int_f NNPS(f)\times df} \qquad (2)$$

where f is the spatial frequency. The noise in the image is a random process. The knowledge of MPV and CV allowed the generation of a random image where for each pixel, its corresponding pixel value was randomly selected assuming the signal statistics can be described by a normal distribution with mean value MPV and standard deviation MPV×CV. The random image generation was performed with the MATLAB function normrnd(MPV, MPV×CV) [6]. This creates a noise image (NI) [4].

The detector also imposes blur in the final image. This blur is characterized by the modulation transfer function (MTF(f)) in the spatial frequency domain and with the point spread function (PSF(x,y)) in the spatial domain. Provided the PSF is known the final image can be created by the convolution of PSF with NI. The knowledge of PSF cannot be directly obtained in literature for a specific detector. On the other hand, MTF can be calculated via the Fourier Transform of a PSF integral with the following formula:

$$MTF(f) = Fourier\left\{\int_x PSF(x,y)dx\right\} \qquad (3)$$

In this work, various shaped curves for generating a PSF(x.y) function, like Gaussian, exponential, hyperbolic and their combinations were tested by trial-and-error method. The resulted PSF of choice was that which yield the closest MTF(f) with the one found in literature.

2.4. Detector parameters selection

The Dexela 2923 mammographic detector with a pixel size of 75 μm was selected. For this detector its MPV function, the MTF curve and NNPS curves for various exposure conditions were available from literature [5]. The final images extracted as 8 bit images.

3. Results

The K to MPV, relationship for Dexela 2923 detector was obtained as [5]: MPV=86.9×K+142.05. By implementing Equation 2 in the published NNPS data it was obtained that the CV is affected by K as: $CV=0.0251\times K^{-0.52}$ [8]. The K values calculated under the mammary gland ranged from 19.8 μGy up to 104.57 μGy well within the linear range of the detector response. Finally, by trial-and-error method it was found that the rotation of the equation $\frac{e^{\frac{-r}{5}}}{(r^2+1.1)^2}$ yields a PSF whose MTF is comparable with the published one. In Figure 2, a comparison of the experimental MTF and the one theoretically determined by equation 3 is demonstrated.

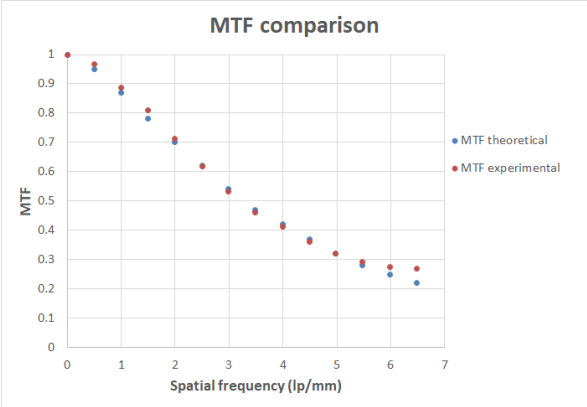

Figure 2. The MTF comparison between the experimentally determined and the one theoretically calculated in this work.

It may be observed from Figure 2 that our MTF underestimates the detector performance in high spatial frequencies. The overall difference between the MTFs is 1.7% and the difference in the high spatial frequency of 6.48 lp/mm is 22.5%.

3.1. Phantom thickness of 5.2 cm

In Figures 3-6 two examples of irradiating the 5.2 cm mathematical simulated phantom with energy 22 keV and X-ray fluence of $4.5x10^6$ photons/mm² are demonstrated. The rectangular lesion thicknesses vertically observed from top to bottom for Figure 3 are: a) for blood 0.5 cm the first and second, 0.4 cm the third, fourth and fifth and 0.3 cm the sixth and seventh, b) for Ca 0.01 cm the first and second, 0.075 cm the third, fourth and fifth and 0.005 cm the sixth and seventh. The corresponding thicknesses for Figure 5 are: a) for blood 0.1 cm the first and second, 0.09 cm the third, fourth and fifth and 0.08 cm the sixth and seventh, b) for Ca 0.001 cm the first and second, 0.0009 cm the third, fourth and fifth and 0.0008 cm the sixth and seventh.

Figure 3. Simulated mathematical image of 5.2 cm phantom thickness irradiated with 22 keV and $4.5×10^6$ photons/mm², with blood thicknesses ranging from 0.5 cm to 0.3 cm and Ca thicknesses ranging from 0.01 cm to 0.005 cm.

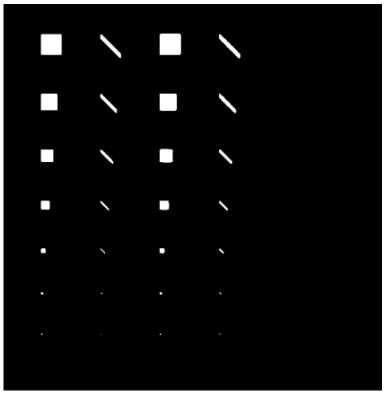

Figure 4. Simulated mathematical image of 5.2 cm phantom thickness irradiated with 22 keV and $4.5x10^6$ photons/mm², with blood thicknesses ranging from 0.5 cm to 0.3 cm and Ca thicknesses ranging from 0.01 cm to 0.005 cm, adjusted with ImageJ from Figure 3.

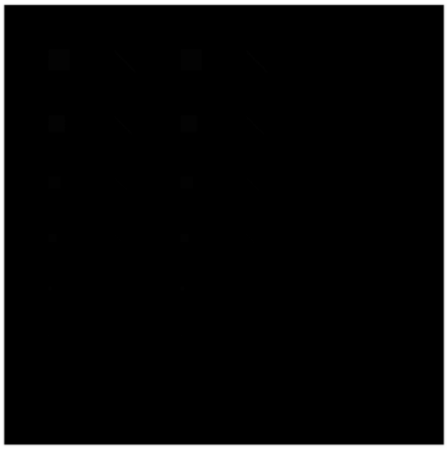

Figure 5. Simulated mathematical image of 5.2 cm phantom thickness irradiated with 22 keV and $4.5×10^6$ photons/mm², with blood thicknesses ranging from 0.1 cm to 0.08 cm and Ca thicknesses ranging from 0.001 cm to 0.0008 cm.

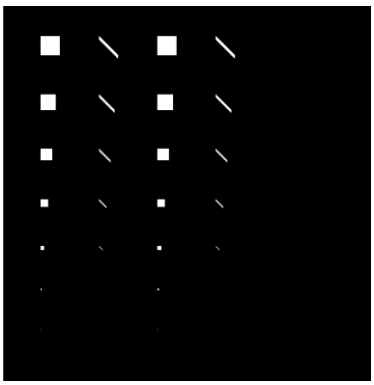

Figure 6. Simulated mathematical image of 5.2 cm phantom thickness irradiated with 22 keV and $4.5×10^6$ photons/mm², with blood thicknesses ranging from 0.1 cm to 0.08 cm and Ca thicknesses ranging from 0.001 cm to 0.0008 cm, adjusted with ImageJ from Figure 5.

Figure 4 and Figure 6 are under the same conditions as Figure 3 and Figure 5 respectively, but are viewed

under the maximum available contrast enhancing window with ImageJ software [9], [10]. It can be seen that Figures 4 and 6 demonstrate more details than Figure 3 and Figure 5. This suggest that the detector under consideration was capable of resolving smaller thicknesses that the ones observed by the eye if no enhancing is performed.

Table 1. Number of visible blood and Ca ROIs and lines for 5.2 cm phantom thickness. The simulated thicknesses ranged from 0.5 cm - 0.3 cm for blood and from 0.01 cm – 0.005 cm for Ca.

System	Blood ROIs	Blood lines	Ca ROIs	Ca lines
Image of 22 keV 4.5×10⁶ photons/mm².	6	5	6	6
Image of 22 keV 6×10⁶ photons/mm².	7	7	7	7
Image of 22 keV 9×10⁶ photons/mm².	7	7	7	7
Image of 28 keV 4.5×10⁶ photons/mm².	7	7	7	7
Image of 28 keV 6×10⁶ photons/mm².	7	7	7	7
Image of 28 keV 9×10⁶ photons/mm².	7	7	7	7

Table 2. Number of visible blood and Ca ROIs and lines for 5.2 cm phantom thickness. The simulated thicknesses ranged from 0.3 cm - 0.1 cm for blood and from 0.005 cm – 0.001 cm for Ca.

System	Blood ROIs	Blood lines	Ca ROIs	Ca lines
Image of 22 keV 4.5×10⁶ photons/mm².	7	7	7	7
Image of 22 keV 6×10⁶ photons/mm².	7	7	7	7
Image of 22 keV 9×10⁶ photons/mm².	7	7	7	7
Image of 28 keV 4.5×10⁶ photons/mm².	6	5	6	5
Image of 28 keV 6×10⁶ photons/mm².	6	5	6	5
Image of 28 keV 9×10⁶ photons/mm²	6	5	6	5

Table 3. Number of visible blood and Ca ROIs and lines for 5.2 cm phantom thickness. The simulated thicknesses ranged from 0.1 cm - 0.08 cm for blood and from 0.001 cm – 0.0008 cm for Ca.

System	Blood ROIs	Blood lines	Ca ROIs	Ca lines
Image of 22 keV 4.5×10⁶ photons/mm².	7	5	7	5
Image of 22 keV 6×10⁶ photons/mm².	7	5	7	5
Image of 22 keV 9×10⁶ photons/mm².	7	5	7	5
Image of 28 keV 4.5×10⁶ photons/mm².	5	3	5	3
Image of 28 keV 6×10⁶ photons/mm².	5	4	5	4
Image of 28 keV 9×10⁶ photons/mm².	5	4	5	4

In Table 1, Table 2 and Table 3 the number of the observed lesions with a maximum contrast window as processed by ImageJ are demonstrated. The lesions are numbered from top to bottom and correspond to the phantom image of Figure 1. Three simulations for each exposure conditions were performed each one with different lesion thicknesses. For the simulation demonstrated in Table 1 the first and second blood lesion of the simulated phantom corresponds to blood thickness of 0.5 cm, the third, fourth and fifth blood lesion of the simulated phantom correspond to blood thickness of 0.4 cm and the sixth and seventh lesion the simulated phantom correspond to blood thickness, of 0.3 cm. The corresponding Ca thicknesses were 0.01, 0.075 and 0.005 respectively. The corresponding lesion thicknesses for the images whose number of visible lesions is demonstrated in Table 2, are for blood 0.3 cm, 0.2 cm and 0.1 cm and for Ca 0.005 cm, 0.003 cm and 0.001 cm. Finally, the corresponding lesion thicknesses for the images whose number of visible lesions is demonstrated in Table 3, are for blood 0.1 cm, 0.09 cm and 0.08 cm and for Ca 0.001 cm, 0.0009 cm and 0.0008 cm respectively.

3.2. Phantom thickness of 6 cm

In Figure 7, the irradiation of a 6 cm thickness phantom with energy 22 keV and X-ray fluence of 9x10⁶ photons/mm² is demonstrated. The rectangular lesion thicknesses vertically observed from top to bottom for Figure 7 are: a) for blood 0.5 cm the first and second, 0.4 cm the third, fourth and fifth and 0.3 cm the sixth and seventh, b) for Ca 0.01 cm the first and second, 0.075 cm the third, fourth and fifth and 0.005 cm the sixth and seventh. In Figure 8 the same image under contrast conditions modified with ImageJ software is demonstrated.

Figure 7. Simulated mathematical image of 6 cm phantom thickness irradiated with 22 keV and 9×10⁶ photons/mm², with blood thicknesses ranging from 0.5 cm to 0.3 cm and Ca thicknesses ranging from 0.01 cm to 0.005 cm.

In Figure 9, the irradiation of a 6 cm thickness phantom with energy 28 keV and X-ray fluence of 4.5x10⁶ photons/mm² is demonstrated. The rectangular lesion thicknesses vertically considered from top to bottom for Figure 9 are: a) for blood 0.1 cm the first and second, 0.09 cm the third, fourth and fifth and 0.08 cm the sixth and seventh, b) for Ca 0.001 cm the first and

second, 0.075 cm the third, fourth and fifth and 0.005 cm the sixth and seventh. Additionally, Figure 10, is the image produced from Figure 9 when applying the maximum available contrast enhancement by ImageJ software.

It Table 4, Table 5 and Table 6 the number of the observed lesions with a maximum contrast window as processed by ImageJ are demonstrated. The corresponding lesion thicknesses for the three irradiation cases are the same as in the 5.2 cm irradiation conditions.

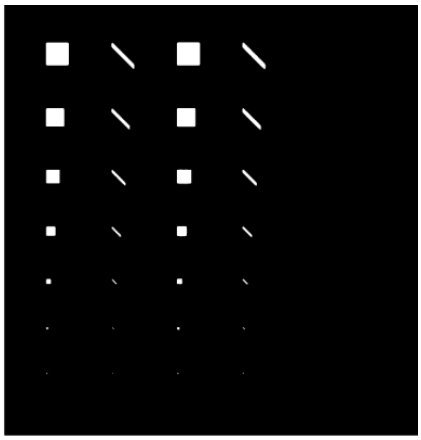

Figure 8. Simulated mathematical image of 6 cm phantom thickness irradiated with 22 keV and 9×10⁶ photons/mm², with blood thicknesses ranging from 0.5 cm to 0.3 cm and Ca thicknesses ranging from 0.01 cm to 0.005 cm, adjusted with ImageJ from Figure 7.

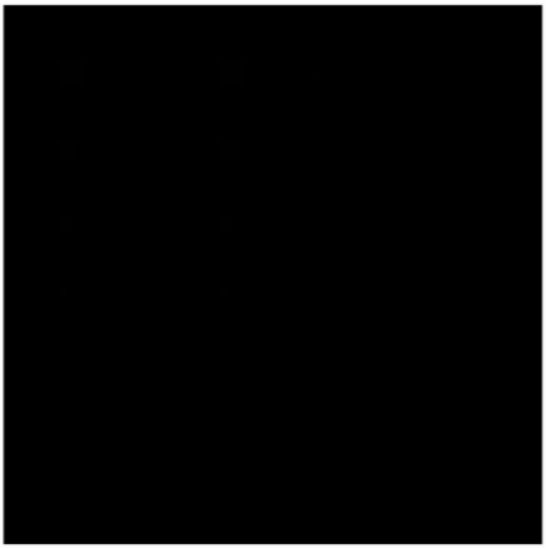

Figure 9. Simulated mathematical image of 6 cm phantom thickness irradiated with 28 keV and 4.5×10⁶ photons/mm², with blood thicknesses ranging from 0.1 cm to 0.08 cm and Ca thicknesses ranging from 0.001 cm to 0.0008 cm.

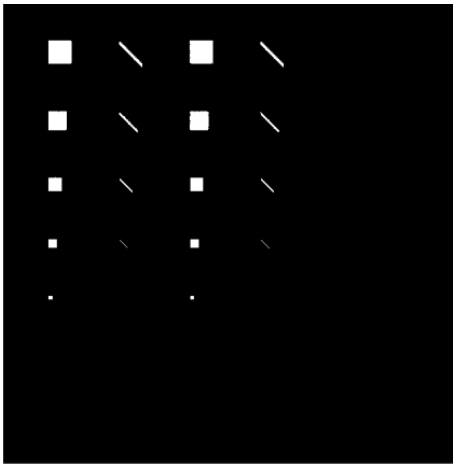

Figure 10. Simulated mathematical image of 6 cm phantom thickness irradiated with 28 keV and 4.5×10⁶ photons/mm², with blood thicknesses ranging from 0.1 cm to 0.08 cm and Ca thicknesses ranging from 0.001 cm to 0.0008 cm, adjusted with ImageJ from Figure 9.

Table 4. Number of visible blood and Ca ROIs and lines for 6 cm phantom thickness. The simulated thicknesses ranged from 0.5 cm - 0.3 cm for blood and from 0.01 cm – 0.005 cm for Ca.

System	Blood ROIs	Blood lines	Ca ROIs	Ca lines
Image of 22 keV 4.5×10⁶ photons/mm².	7	7	7	7
Image of 22 keV 6×10⁶ photons/mm².	7	7	7	7
Image of 22 keV 9×10⁶ photons/mm².	7	7	7	7
Image of 28 keV 4.5×10⁶ photons/mm².	7	7	7	7
Image of 28 keV 6×10⁶ photons/mm².	7	7	7	7
Image of 28 keV 9×10⁶ photons/mm².	7	7	7	7

Table 5. Number of visible blood and Ca ROIs and lines for 6 cm phantom thickness. The simulated thicknesses ranged from 0.3 cm - 0.1 cm for blood and from 0.005 cm – 0.001 cm for Ca.

System	Blood ROIs	Blood lines	Ca ROIs	Ca lines
Image of 22 keV 4.5×10⁶ photons/mm².	7	7	7	7
Image of 22 keV 6×10⁶ photons/mm².	7	7	7	7
Image of 22 keV 9×10⁶ photons/mm².	7	7	7	7
Image of 28 keV 4.5×10⁶ photons/mm².	6	5	6	5
Image of 28 keV 6×10⁶ photons/mm².	6	5	6	5
Image of 28 keV 9×10⁶ photons/mm².	6	5	6	5

Table 6. Number of visible blood and Ca ROIs and lines for 6 cm phantom thickness. The simulated thicknesses ranged from 0.1 cm - 0.08 cm for blood and from 0.001 cm – 0.0008 cm for Ca.

System	Blood ROIs	Blood lines	Ca ROIs	Ca lines
Image of 22 keV 4.5×10⁶ photons/mm².	7	5	7	5
Image of 22 keV 6×10⁶ photons/mm².	7	5	7	5
Image of 22 keV 9×10⁶ photons/mm².	7	5	7	5
Image of 28 keV 4.5×10⁶ photons/mm².	5	3	5	3
Image of 28 keV 6×10⁶ photons/mm².	5	4	5	4
Image of 28 keV 9×10⁶ photons/mm².	5	4	5	4

4. Discussion

It can be observed from Tables 1 to 6 that the thin objects at 28 keV exposure conditions present reduced detectability even with the maximum contrast settings. This occurs because the X-ray attenuation coefficients of blood and Ca are closer to the X-ray attenuation coefficient of the breast at 28 keV with respect to the corresponding ones at 22 keV. More specifically at 22 keV the linear attenuation coefficient of breast tissue, blood tissue and Ca are 0.576 cm^{-1}, 0.721 cm^{-1} and 15.4 cm^{-1} respectively. The corresponding coefficients at 28 keV are 0.381 cm^{-1}, 0.455 cm^{-1} and 7.68 cm^{-1}. The smaller difference at 28 keV suggests smaller differences in the calculation of $e^{-\mu_1 \times T}$ and $e^{-\mu_1 \times (T-t)} e^{-\mu_2 \times t}$ values. This is more profound when small lesion thicknesses, $t<<T$ are examined. However, the image visual detection, before ImageJ contrast enhancement, depends upon pixel value differences in the images originally produced. In Figure 11 and Figure 12 the pixel value differences of the blood lesions, with thicknesses ranged from 0.08 cm to 0.5 cm, and Ca lesions, with thicknesses ranged from 0.0008 cm to 0.01 cm, with the breast tissue are demonstrated. The corresponding differences after ImageJ contrast enhancement were over 250 for the 8-bit level images created in this study.

Besides the exposure conditions the effect of the detector is more pronounced at small signal differences as well at small object sizes. The image noise introduced may hinder the visibility of low contrast difference objects like blood and breast tissue. The increased X-ray fluence results in reduced image noise. This seems to improve lesion visualization at Table 1, Table 3 and Table 6 cases. In addition, the blur introduced be the PSF function combined with the image noise may further prevent the imaging system to resolve small objects. This is more evident in the small thickness line images at 28 keV, as well as at the 4×4 pixels and 2×2 pixels square regions where the combined effect of higher energy and the detector blur and noise properties obstruct the lesion resolve in the image. However, due the reduced MTF values at high spatial frequences of the simulated MTF with respect to the experimental one, our results may underestimate the detector performance when small size lesions are imaged.

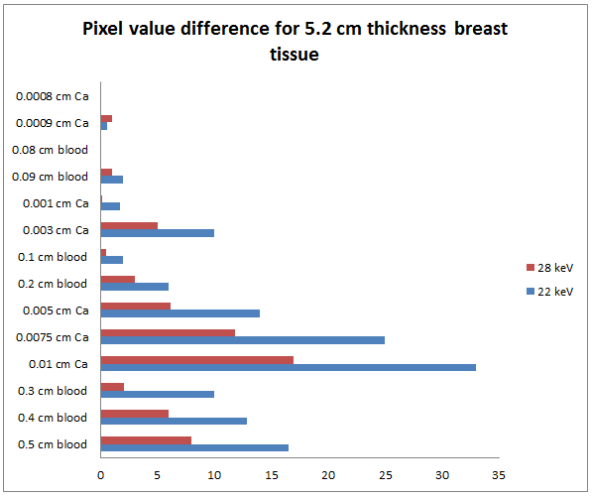

Figure 11. Pixel value difference between the 5.2 cm phantom thickness and the lesions under consideration in this study. at 9×10⁶ photons/mm².

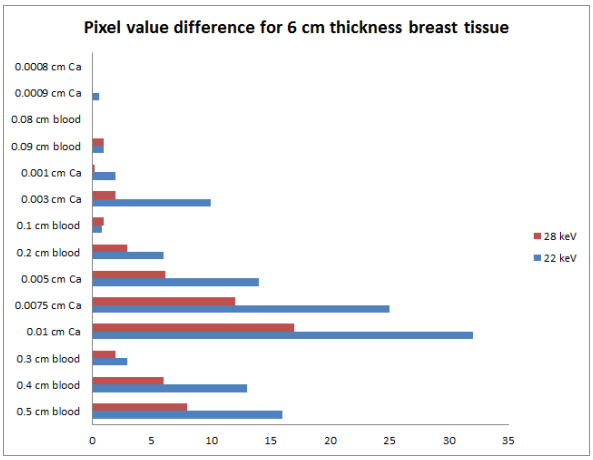

Figure 12. Pixel value difference between the 6 cm phantom thickness and the lesions under consideration in this study. at 9×10⁶ photons/mm².

5. Conclusion

A mathematical phantom was used to simulate the imaging capabilities of a digital detector. It was found that the detector could resolve the 2×2 pixels size Ca lesions at 6 cm thickness breasts corresponding to 150 μm × 150 μm size and 0.001 cm thickness at both 22 keV and 28 keV.

References

1. W. Ren, M. Chen, Y. Qiao, F. Zhao. "Global guidelines for breast cancer screening: A systematic review," *Breast*, vol. 64, pp. 85 – 99, Aug. 2022. DOI: 10.1016/j.breast.2022.04.003 PMid: 35636342 PMCid: PMC9142711

2. H. Aichinger, J. Dierker, S. Joite-Barfuß, M. Säbel, "Principles of X-Ray Imaging," in *Radiation Exposure and Image Quality in X-ray Diagnostic Radiology: Physical Principles and Clinical Applications*, 2nd ed., Berlin Heidelberg, Germany: Springer-Verlag, 2012, ch. 1, pp. 3 – 7.
DOI: 10.1007/978-3-642-11241-6_1
3. K. Bliznakova "The advent of anthropomorphic three-dimensional breast phantoms for X-ray imaging," *Phys. Med.*, vol. 79, pp. 145 – 161, Nov. 2020.
DOI: 10.1016/j.ejmp.2020.11.025
PMid: 33321469
4. N. Kalyvas et al., "A Novel Method to Model Image Creation Based on Mammographic Sensors Performance Parameters: A Theoretical Study," *Sensors*, vol. 23, no. 4, 2335, Feb. 2023.
DOI: 10.3390/s23042335
PMid: 36850937
PMCid: PMC9968010
5. A. C. Konstantinidis, M. B. Szafraniec, R. D. Speller, A. Olivo "The Dexela 2923 CMOS X-ray detector: A flat panel detector based on CMOS active pixel sensors for medical imaging applications," *Nucl. Instrum. Methods in Phys. Res. Sec. A*, vol. 689, pp. 12 – 21, Oct. 2012.
DOI: 10.1016/j.nima.2012.06.024
6. *MATLAB version 9.12*, MathWorks, Natick (MA), USA, 2022.
Retrieved from: https://www.mathworks.com
Retrieved on: Jun. 30, 2025
7. R. Nowotny, *XMuDat: Photon attenuation data on PC version 1.0.1*, IAEA Nuclear Data Section, Vienna, Austria, 1998.
Retrieved from:
https://www-nds.iaea.org/publications/iaea-nds/iaea-nds-0195.htm
Retrieved on: Jun. 30, 2025
8. S. Katsanevaki, "Mathematical creation of a phantom to study the effect of exposure on mammography," Diploma Thesis, University of West Attica, Athens, Greece, 2024.
DOI: 10.26265/polynoe-5930
9. W. Rasband, *ImageJ version 1.47h*, National Institutes of Health, Bethesda (MD), USA, 2012.
Retrieved from:
https://imagej.net/ij/
Retrieved on: Jun. 30, 2025
10. F. Stossi, P. K. Singh, "Basic Image Analysis and Manipulation in ImageJ/Fiji," *Curr. Protoc.*, vol. 3, no. 7, e849, Jul. 2023.
DOI: 10.1002/cpz1.849
PMid: 37498127